The TWK-26 potassium channel governs nutrient absorption in the *C. elegans* intestine

Sarah K. Torzone[1], Peter C. Breen[1], Natalie R. Cohen[1], Kaylee N. Simmons[1], Robert H. Dowen[1,2,3*]

[1]Integrative Program for Biological and Genome Sciences, The University of North Carolina at Chapel Hill, Chapel Hill, North Carolina, United States of America

[2] Department of Biology, The University of North Carolina at Chapel Hill, Chapel Hill, North Carolina, United States of America

[3] Department of Cell Biology and Physiology, The University of North Carolina at Chapel Hill, Chapel Hill, North Carolina, United States of America

* Corresponding author

E-mail: dowen@email.unc.edu

ABSTRACT

Ion channels are necessary for proper water and nutrient absorption in the intestine, which supports cellular metabolism and organismal growth. While a role for Na^+ co-transporters and pumps in intestinal nutrient absorption is well defined, how individual K^+ uniporters function to maintain ion homeostasis is poorly understood. Using *Caenorhabditis elegans*, we show that a gain-of-function mutation in *twk-26*, which encodes a two-pore domain K^+ ion channel orthologous to human KCNK3, facilitates nutrient absorption and suppresses the metabolic and developmental defects displayed by impaired intestinal MAP Kinase (MAPK) signaling. Mutations in *drl-1* and *flr-4,* which encode two components of this MAPK pathway, cause severe growth defects, reduced lipid storage, and a dramatic increase in autophagic lysosomes, which mirror dietary restriction phenotypes. Additionally, these MAPK mutants display structural defects of the intestine and an impaired defecation motor program. We find that activation of TWK-26 reverses the dietary restriction-like state of the MAPK mutants by restoring intestinal nutrient absorption without correcting the intestinal bloating or defecation defects. This study provides unique insight into the mechanisms by which intestinal K^+ ion channels support intestinal metabolic homeostasis.

INTRODUCTION

Ion channels are membrane proteins that regulate the excitability of specialized cells that generate and propagate action potentials, as well as cell types that generate ion gradients to govern water, electrolyte, and small molecule transport across membranes. In the intestine, maintenance of membrane potential and transmembrane ion gradients is essential for nutrient absorption and digestion (Lu et al. 2023). Dysregulation of ion channel expression or function in intestinal enterocytes contributes to several gastrointestinal (GI) pathologies, as seen in cystic fibrosis, colonic inflammation, and colorectal cancers (Anderson et al. 2019). For example, intermediate conductance potassium ion (IK) channels on the basolateral membrane of colonocytes are required for membrane hyperpolarization which supports Na^+ and Cl^- transport across the cell membrane, which, when impaired, results in diseases such as ulcerative

colitis (Al-Hazza et al. 2012). Consistently, decreased expression of basolateral IK channels in inflammatory bowel disease results in secretion of K^+ ions into the intestinal lumen, causing abdominal pain and diarrhea (Magalhães et al. 2016). Because ion channels are essential for preserving gastrointestinal function and organismal energy homeostasis, it is crucial to understand the molecular regulation of their activity to identify novel therapeutic targets of GI disease.

The depolarization or hyperpolarization of intestinal epithelial cells (IECs) is largely responsible for tuning the activity of nutrient transporters (Lu et al. 2023). For example, transport of peptides by the di/tripeptide nutrient transporter PepT1 requires the recycling of a H^+ ion gradient across the apical membrane of IECs (Thwaites et al. 2002). Thus, proper nutrient absorption in the intestine is pH dependent. The electrogenic forces that drive proton-coupled amino acid and glucose absorption in IECs are often stabilized by K^+ channels, although little is known about the role of potassium ion channels in lipid absorption (Lu et al. 2023). Moreover, how specific potassium ion channels regulate metabolic processes in the intestine to promote organismal homeostasis remains poorly understood.

Regulation of intestinal nutrient absorption by ion gradients is well conserved. In the nematode *Caenorhabditis elegans*, 20 identical epithelial cells absorb all the lipids, peptides, and carbohydrates required to maintain metabolic homeostasis and promote growth. The *C. elegans* gene *pept-1* encodes an intestinal oligopeptide transporter that is the ortholog of mammalian PepT1. As the primary di/tri-peptide transporter in the intestine, loss of *pept-1* impairs amino acid uptake, which slows development and reduces body size in *C. elegans* (Nehrke 2003). Likewise, loss of the apical Na^+/H^+ exchanger NHX-2/NHE3, an intestinal antiporter that maintains intestinal acidification and drives pH-dependent nutrient absorption, impairs growth and development (Nehrke 2003). Furthermore, disruption of *nhx-2* blunts lipid absorption, possibly arising from PEPT-1-dependent intracellular acidification (Spanier et al. 2009).

Intestinal pH oscillations, which support nutrient absorption and metabolic homeostasis, are also necessary to promote a rhythmic defecation cycle in *C. elegans*. The *C. elegans* defecation motor program (DMP) occurs every ~45 seconds and is coordinated by calcium and proton oscillations in the intestine

(Allman et al. 2009; Pfeiffer et al. 2008). The DMP is coupled to absorption of essential nutrients, including dipeptides, glucose, and lipids (Allman et al. 2009; Sheng et al. 2015; Suzuki et al. 2022). Consistently, mutations that disrupt the DMP (e.g., *aex-5* and *flr-1*) reduce somatic intracellular lipid stores (Kaulich et al. 2022; Sheng et al. 2015), likely due to impaired intestinal acidification and poor nutrient absorption. Although maintenance of intestinal ion homeostasis is imperative to the overall metabolic health of the organism, as it governs both defecation and nutrient absorption, little is known about the molecular regulation of these processes.

We previously demonstrated that DRL-1 and FLR-4, two intestinal protein kinases that function in a mitogen-activated protein kinase (MAPK) signaling pathway, promote growth, lipid accumulation, and reproduction in *C. elegans* by, at least in part, suppressing the p38 innate immune pathway (Torzone et al. 2023). Mutations in *drl-1*, which is also known as *flr-3* (Honey et al. 2023), *flr-4*, and *flr-1*, which encodes a degenerin (DEG)/epithelial sodium channel (ENaC), were identified in a forward genetic screen for genetic lesions that confer resistance to fluoride (Katsura et al. 1994). Intriguingly, mutations in *drl-1*, *flr-4*, and *flr-1* all disrupt the DMP, cause developmental delay, and reduce lipid stores (Chamoli et al. 2014; Katsura et al. 1994; Kaulich et al. 2022; Take-uchi et al. 1998, 2005; Torzone et al. 2023), suggesting that MAPK signaling and ion channels may function in concert to coordinate defecation, metabolism, and development; however, the mechanistic basis of this regulation is unknown.

In this study, we identify a gain-of-function mutation in the *twk-26* gene, which encodes a potassium two-pore domain (K2P) ion channel, that suppresses the metabolic and developmental defects conferred by the *flr-4* and *flr-1* mutations. Furthermore, we find that loss of *flr-4* and *flr-1* severely impairs intestinal nutrient absorption, which is restored when TWK-26 is activated. Remarkably, the *twk-26* gain-of-function mutation fails to suppress the defects in the defecation motor program displayed by *flr-4* and *flr-1* mutants, demonstrating that nutrient absorption can be uncoupled from the DMP. Our study provides new mechanistic insight into the dual regulation of intestinal metabolism by K^+ ion homeostasis and MAPK signaling.

RESULTS

A gain-of-function mutation in a potassium channel reverses the metabolic defects conferred by impaired MAPK signaling

The *flr-4* gene encodes a protein orthologous to the mammalian STK25 kinase, a member of the germinal center kinase III (GCK III) subfamily and Ste20 superfamily of kinases (Torzone et al. 2023). STK25 promotes lipid accumulation in hepatocytes and its overexpression has been observed in hepatocellular carcinoma patients and is associated poor clinical outcomes (Amrutkar et al. 2016; Zhang et al. 2022). Consistently, intestinal FLR-4 promotes growth and maintains lipid homeostasis in *C. elegans*, partially through regulation of the p38 MAPK pathway (Torzone et al. 2023). Additionally, *flr-4* is required for maximal expression of the intestinal vitellogenin proteins (VIT-1-6), which mediate the transport of lipids to mature oocytes via lipoprotein particles thereby supporting reproduction and embryonic development (Kimble and Sharrock 1983; Torzone et al. 2023). Consistently, loss of *flr-4*, or its kinase activity, results in a striking reduction in the body size and intestinal vitellogenin expression.

The downstream targets of FLR-4, which may be other kinases that act within a canonical signaling cascade, are unknown. Expression of the P*vit-3::GFP* vitellogenesis reporter, which consists of the *vit-3* promoter driving GFP (Dowen et al. 2016), is markedly down-regulated after loss of *flr-4*. Leveraging this vitellogenesis phenotype, we sought to identify additional components of this MAPK signaling pathway by conducting a forward genetic screen for mutations that suppress the P*vit-3::GFP* expression defects in the *flr-4(ut7)* mutant (Figure 1A). We specifically targeted suppressors in the F1 generation to enrich for gain-of-function suppressor mutations. Following backcrossing to the non-mutagenized strain, we performed whole genome sequencing of the suppressor mutants and identified candidate causative mutations using computational approaches. Remarkably, we identified four, independently generated, instances of the same mutation in *twk-26*, which encodes a two-pore domain potassium (K2P) ion channel (Figure 1A). The *C. elegans* genome encodes 47 K2P channels, most of which have unknown functions (Hobert 2013), including *twk-26*. K2P channels are a class of potassium

leak channels that possess four transmembrane domains and two pore-forming domains (Feliciangeli et al. 2015). The TOPCONS consensus prediction (Tsirigos et al. 2015) of TWK-26 identified four transmembrane domains (Figure 1B), which is consistent with the structure of other K2P channels. The mutation in TWK-26, G485E, is positioned within the C- terminus proximal to the final transmembrane domain. A role for TWK-26 in lipid metabolism is surprising, as potassium ion leak channels are known to play a role in neurotransmission and vascular tone modulation in mammals, but little is known about their role outside of these excitable tissues (Feliciangeli et al. 2015).

To further elucidate the role of TWK-26 in growth and metabolic homeostasis, we compared the developmental rate of the *flr-4(ut7)* single mutant to the *flr-4(ut7); twk-26(rhd182[G485E])* double mutant. Interestingly, the *twk-26* allele fully suppressed the developmental delay of the *flr-4* mutant when animals were consuming *E. coli* OP50; however, *twk-26(rhd182)* was only a weak suppressor of *flr-4* when animals were fed *E. coli* HT115 (Figure 1C), suggesting that a nutritional component may alter signaling through this pathway. We previously demonstrated that loss of FLR-2, a neuronally-expressed glycoprotein hormone, its receptor, FSHR-1, or downstream cAMP signaling suppressed the growth and metabolic defects displayed by the *flr-4* mutant (Torzone et al. 2023). The *twk-26(rhd182[G485E])* allele suppressed the defects in body size, lipid storage, and vitellogenesis displayed by the *flr-4(ut7)* mutant, as we observed with the *flr-2* mutation (Figures 1D-G and S1A). Total lipid levels, as determined by Oil Red O and Nile Red staining, and vitellogenin expression, measured using a single-copy P*vit-3::mCherry* transcriptional reporter, was not fully restored to wild-type levels by the *twk-26* mutation, nor was this mutation as strong of a suppressor as *flr-2*. Together, these results reveal that *twk-26* plays an important role in regulating MAPK-mediated growth and lipid metabolism.

The *flr-4(ut7)* allele, as well as mutations in *flr-1* and *flr-3*/*drl-1*, were isolated in a forward genetic screen for mutations that confer resistance to fluoride (Katsura et al. 1994). FLR-1, an acid-sensing sodium ion channel, and FLR-4 are known to function together in the intestine, whereby the C-terminus of FLR-4 maintains the expression of FLR-1 (Kobayashi et al. 2011). Additionally, DRL-1 and FLR-4

form a protein kinase complex in the intestine (Torzone et al. 2023). Thus, we reasoned that if *twk-26(rhd182)* suppressed the *flr-4(ut7)* mutation, it may also suppress *flr-1* and *drl-1* mutations. Indeed, the *twk-26(rhd182)* allele fully suppressed the reduced growth rate, as well as modestly suppressed the impaired P*vit-3::mCherry* reporter expression, of the *flr-1* and *drl-1* mutants (Figure S1B-C). Consistent with our previous results, suppression by *twk-26* was observed in *E. coli* OP50-fed animals, but not in those consuming *E. coli* HT115. Additionally, *twk-26(rhd182)* suppressed the lipid storage and body size defects of the *flr-1* mutant to similar levels as the *flr-2* mutation (Figure S1D-E), suggesting that the metabolic and growth defects associated with loss of FLR-1 is due to impaired ion homeostasis. Together, our data indicate that the TWK-26 K2P-encoding protein functions in concert with MAPK signaling to coordinate growth and lipid homeostasis in *C. elegans*.

The *twk-26(G485E)* mutation is a gain-of-function suppressor of *flr-4*

We isolated the *twk-26(rhd182)* allele in the F1 generation of an EMS mutagenesis screen, suggesting that the G485E mutation is confers either a gain-in-function or haploinsufficiency. To differentiate between these two possibilities, we knocked-down *twk-26* by RNAi in *flr-4(ut7)* and *twk-26(rhd182); flr-4(ut7)* mutant animals and assessed the resulting phenotypes. If *twk-26(rhd182)* is a loss-of-function allele, *twk-26* RNAi would suppress the growth rate, body size, and metabolic defects observed in *flr-4(ut7)* mutants; however, if *twk-26(rhd182)* is a gain-of-function allele, *twk-26* RNAi would impair the suppressive effects that we observed in the *twk-26(rhd182); flr-4(ut7)* animals. Knock-down of *twk-26* abrogated the suppressive effects of *twk-26(rhd182)*, producing animals with slowed developmental rates and small body sizes that is characteristic of the *flr-4* mutation (Figure 2A-C). Interestingly, the *twk-26(rhd182)* allele failed to suppress the vitellogenesis defects in the *flr-4(ut7)* mutant when animals were fed control *E. coli* HT115 RNAi bacteria (Figure S2A), which is consistent with our previous findings that *twk-26(rhd182)* does not effectively suppress the *flr-4* mutation when reared on *E. coli* HT115. Notably, the *twk-26(rhd182)* mutation alone significantly reduced P*vit-*

3::mCherry reporter expression, which was reversed by *twk-26* RNAi (Figure S2A). Together, these data indicate that the *twk-26(rhd182[G485E])* allele is a gain-of-function allele, providing unique molecular insight into our understanding of the TWK-26 K2P channel. Presumptive activation, and not loss, of the ion channel reverses the dramatic developmental and metabolic defects of the *flr-4(ut7)* mutants.

A predicted human ortholog of TWK-26 is KCNK3/TASK, a two-pore domain K^+ leak channel that is broadly expressed, including in the brain and small intestine, and that is strongly inhibited by extracellular acidification (Duprat et al. 1997). Interestingly, KCNK3 gain-of-function mutations increase channel opening probability and are associated with developmental disorders with sleep apnea (Sörmann et al. 2022). KCNK3 contains a structural motif called the X-gate, which regulates the opening and closing of the channel (Rödström et al. 2020). The KCNK3 G129D mutation is a gain-of-function allele identified in several sleep apnea patients that destabilizes the X-gate, resulting in increased current through the channel (Sörmann et al. 2022). Therefore, we reasoned that introduction of this mutation into TWK-26 at the conserved glycine residue may hyperactivate TWK-26 and suppress loss of *flr-4*. To test this hypothesis, we engineered the analogous G236D point mutation into the *twk-26* locus by CRISPR/Cas9 gene editing, depleted FLR-4 using auxin-dependent degradation (Torzone et al. 2023), and assessed P*vit-3::mCherry* expression. Depletion of FLR-4 in wild-type and *twk-26(rhd294[G236D])* backgrounds resulted in a similar decrease in P*vit-3::mCherry* expression (Figure S2B), indicating that the putative G236D gain-of-function mutation does not confer the same effects as the G485E gain-of-function mutation. Consistently, frameshift mutations in the *twk-26* locus generated during CRISPR/Cas9 editing, which we presumed to be full loss-of-function alleles, failed to suppress the defects in *vit* gene expression upon FLR-4 depletion, which is consistent with our RNAi studies. Together, our results argue that the TWK-26 G485E mutation confers a gain-in-function, although in a manner that is distinct from the human KCNK3 G129D mutant, which possesses increased ion conductance.

TWK-26 activation restores intestinal nutrient absorption in the *flr-4* and *flr-1* mutants

We and others have shown that loss of DRL-1 or FLR-4 in the intestine causes a dietary restriction-like (DR-like) state, resulting in small body sizes, slowed development, and impaired lipid homeostasis (Chamoli et al. 2014; Katsura et al. 1994; Torzone et al. 2023). Loss of *flr-1* also results in a DR-like phenotype (Kaulich et al. 2022; Oishi et al. 2009; Take-uchi et al. 1998), which is consistent with our findings (Figure S1B-E). Given the similarity between the mutant phenotypes, it is likely that *flr-1*, *drl-1*, and *flr-4* act in the same pathway to maintain metabolic homeostasis. Moreover, these DR-like phenotypes are all partially suppressed by the *twk-26* gain-of-function mutation, suggesting that impaired ion homeostasis may be contributing to the DR-like phenotypes that we observed in these mutants.

Two-pore domain potassium leak channels, like TWK-26, are known to stabilize the ion gradients that drive electrogenic nutrient transport in the intestine (Lu et al. 2023). Thus, it is plausible that *twk-26(rhd182[G485E])* suppresses the lipid storage defects of the *flr* mutants by enhancing the absorption of fatty acids in the intestine. To test this hypothesis, we fed worms C1-BODIPY-C12, a fluorescently-labeled fatty acid derivative, to track lipid uptake in the intestine of the *flr-4* and *flr-1* mutants (O'Rourke et al. 2009; Sheng et al. 2015; Spanier et al. 2009). Remarkably, loss of *flr-4* or *flr-1* resulted in a striking reduction in the uptake of BODIPY-labelled fatty acids from the intestinal lumen compared to wild-type animals (Figures 3A-B), suggesting that *flr-4* and *flr-1* are crucial for intestinal lipid absorption. This defect may underlie the DR-like state of these mutants. Importantly, lipid absorption is restored when the *twk-26* gain-of-function mutation is introduced into the *flr-4* or *flr-1* mutant backgrounds. Consistently, *flr-4* mutants consuming Nile Red, a lysochrome dye that accumulates in intestinal lipid droplets and lysosome-related organelles following absorption (O'Rourke et al. 2009), displayed significantly less Nile Red signal in the intestine compared to the wild-type controls and the *twk-26(rhd182*); *flr-4* double mutant (Figure S3). Together, these data suggest that the DR-like state of the *flr* mutants may be caused by impaired nutrient absorption caused by loss of intestinal ion homeostasis.

While the lipid storage defects in the *flr-4* and *flr-1* mutants may be largely attributed to poor absorption of fatty acids in the intestine, it is also possible that TWK-26 activation supports the absorption

of additional metabolic resources from the intestinal lumen, including amino acids and carbohydrates. Dipeptides are absorbed in the intestine via the PEPT-1/PepT1 oligopeptide transporter, which when lost results in developmental delay and intestinal morphology defects (Meissner et al. 2004). Furthermore, proper intestinal acidification is required to sustain absorption of dipeptides through PEPT-1 (Allman et al. 2009). Intestinal dipeptide transport is driven by a proton gradient that is established the NHE3 sodium-proton exchanger, known as NHX-2 in *C. elegans* (Nehrke 2003; Thwaites et al. 1999, 2002). Animals that have lost either *nhx-2* or *pept-1* are developmentally delayed (Nehrke 2003), likely due to impaired uptake of dipeptides that are crucial for growth. Therefore, we hypothesized that the *flr-4* and *flr-1* mutants, which are developmentally delayed and have impaired fatty acid absorption, will also show impaired dipeptide absorption that will be restored by the *twk-26* gain-of-function mutation. First, we established that knockdown of *pept-1* or *nhx-2* by RNAi resulted in a decrease in P*vit-3::mCherry* expression and reduced body size (Figures S4A-C), neither of which were suppressed by activation of *twk-26* or loss of *flr-2*, suggesting that *twk-26(rhd182[G485E])* is either genetically upstream of *nhx-2*/*pept-1* or that it restores proper growth and lipid homeostasis in *flr-4* mutants via a mechanism independent of dipeptide transport. Furthermore, if *flr-4* was required for the expression of the *pept-1* or *nhx-2* genes, we would expect that their expression would be lost in the *flr* mutants; however, we observed increased expression of *pept-1* and *nhx-2* in the *flr-4(ut7)* and *drl-1(rhd109)* mutants (Figure S4D), which may be a compensatory mechanism for the cellular starvation that is triggered by loss of these kinases. Together, these data indicate that the FLR-4/DRL-1 MAPK axis is not required for expression of channels involved in dipeptide transport and that TWK-26 likely acts upstream of intestinal peptide absorption.

It is possible that the *twk-26* gain-of-function mutation enhances peptide absorption independently of NHX-2/PEPT-1 by restoring ion homeostasis upon loss of FLR-4 or FLR-1. To test this hypothesis, we directly assessed dipeptide uptake in animals fed β-Ala-Lys(AMCA), a fluorescent dipeptide, by microscopy. Consistent with our lipid absorption studies, mutation of either *flr-4* or *flr-1*

impairs dipeptide absorption; however, the *twk-26(rhd182[G485E])* gain-of-function mutation, as well as the *flr-2* loss-of-function mutation, suppressed these defects (Figure 3C). Together, our results demonstrate that the DRL-1/FLR-4 MAPK signaling pathway and FLR-1 sodium channel govern the absorption of nutrients in the gut, likely by maintaining intestinal ion homeostasis.

Hyperactivation of TWK-26 suppresses autophagy in the nutrient starved *flr* mutants

During starvation, organisms rewire metabolic pathways to initiate catabolic programs, granting access to stored energy reserves when external nutrients are scarce. For example, rapid depletion of intestinal lipids during the initial stages of starvation is a survival mechanism that is conserved across species (Tan et al. 2011). In *C. elegans*, the transcription factor HLH-30, which is orthologous to mammalian TFEB (Lapierre et al. 2013), up-regulates metabolic genes involved in lipolysis during nutrient deprivation (O'Rourke and Ruvkun 2013). Importantly, HLH-30 couples the breakdown of lipid droplet fats with autophagy (O'Rourke and Ruvkun 2013), which shuttles fats from lipid droplets to lysosomes during lipophagy (Singh et al. 2009).

Therefore, we hypothesized that the *flr-4* and *flr-1* mutants, which display a DR-like phenotype likely do to impaired nutrient absorption, would display an enhanced autophagic response that would be suppressed by activation of TWK-26. To test this hypothesis, we used a dual-fluorescent mCherry::GFP::LGG-1 reporter to visualize the induction of autophagy in *twk-26(rhd182)* mutants. The mCherry::GFP::LGG-1 protein, which is orthologous to Atg8, co-labels autophagosomes with mCherry/GFP and autolysosomes with mCherry due to pH quenching of GFP (Chang et al. 2017). Because an increase in autophagic activity is accompanied by an increase in autophagic vesicles (Chang et al. 2017), we quantified the number and size of mCherry-labelled autolysosomes in intestinal cells to assess autophagic flux. We could not visualize an appreciable number of mCherry/GFP punctae, consistent with previous studies that employed this strain (Chang et al. 2017), and therefore, we did not quantify the number of autophagosomes. Importantly, quantification of autolysosomes alone is a sufficient

measure of autophagic activity, given that the mCherry autolysosomes are known to co-localize with LysoTracker (Chang et al. 2017). We found that knockdown of *flr-4* or *flr-1* by RNAi resulted in a dramatic increase in the amount and size of intestinal autolysosomes (Figures 4A-B), indicating an up-regulation of autophagic activity that is likely a response to starvation due to improper nutrient absorption. Importantly, this increase in autophagy is suppressed by *twk-26(rhd182[G485E])*, indicating that activation of TWK-26 suppresses the cellular starvation response to failed nutrient absorption.

Given that loss of *flr-4* and *flr-1* increased autophagic flux, we hypothesized that the HLH-30/TFEB transcription factor, which up-regulates autophagy factors during starvation (Settembre et al. 2013), would accumulate in intestinal nuclei of the *flr* mutants. Surprisingly, knockdown of *flr-4* or *flr-1* by RNAi severely reduced the levels of nuclear HLH-30 (Figure 4C), which was suppressed by *twk-26(rhd182)*. Consistently, knock-down of *hlh-30* by RNAi had little impact on P*vit-3::mCherry* reporter expression nor the body sizes of the *flr-4* or *flr-4; twk-26(rhd182[G485E])* mutants (Figure S5). These results argue that loss of *flr-4* and *flr-1* prompt an HLH-30-independent induction of autophagy. Therefore, we investigated whether the starvation-responsive transcription factor HLH-11/TFAP4 responds to impaired nutrient absorption. HLH-11 suppresses the expression of lipid catabolism genes under well-fed conditions and is degraded during starvation to release fat reserves for energy (Li et al. 2020). Indeed, knock-down of *flr-4* or *flr-1* by RNAi reduced levels of nuclear HLH-11 in the intestine; however, this reduction in HLH-11 nuclear signal was suppressed by the *twk-26(rhd182[G485E])* mutation (Figure 4D), suggesting that TWK-26 activation prevents the degradation of HLH-11 when nutrients are available. Together, these data argue that impaired nutrient absorption due to loss of MAPK signaling stimulates an HLH-30-independent, HLH-11-dependent induction of autophagy.

The TWK-26 G485E mutation uncouples nutrient absorption from the defecation cycle

The *flr-4* and *flr-1* mutants, which exhibit a DR-like state due to nutrient absorption defects, have been previously reported to display an irregular defecation cycle (Iwasaki et al. 1995; Katsura et al. 1994;

Take-uchi et al. 1998, 2005), resulting in a 'constipated' phenotype (Take-uchi et al. 1998). The *C. elegans* defecation motor program (DMP) is a highly coordinated behavior that is temporally regulated, with each DMP occurring every 45 seconds and consisting of 3 steps, which together, last for 5 seconds (Thomas 1990). These steps include the posterior body wall contraction (pBoc), anterior body wall contraction (aBoc), and expulsion, which ultimately results in the release of gut contents. The DMP is controlled by nutritional and environmental inputs, including food availability, temperature, and mechanosensory stimulation (Liu and Thomas 1994). Many of the factors that regulate the DMP have been studied in detail; however, the *flr-4* and *flr-1* mutations shorten the DMP cycle and cause expulsion defects for unclear reasons (Branicky and Hekimi 2006; Iwasaki et al. 1995). The constipated phenotype, which likely results from improper expulsion of gut contents (Liu and Thomas 1994), coincides with intestine bloating (Gruss and Corsi 2022; Lin-Moore et al. 2021). Intestine bloating can be indicative of increased microbial colonization, activation of innate immunity pathways, and initiation of pathogen aversion behaviors (Singh and Aballay 2019). Consistently, a defective DMP is accompanied by intestinal bloating, enhanced susceptibility to pathogens, and DR-like phenotypes (Das et al. 2023).

We hypothesized that the *flr-4* and *flr*-1 mutants would display DMP defects, intestinal bloating, and increased immune signaling, which would be suppressed by *twk-26(rhd182[G485E])*. To test this hypothesis, we first examined the morphology of the intestinal lumen of animals expressing ERM-1::GFP, which localizes to the intestinal apical membrane and facilitates lumen width measurements (Ramalho et al. 2020). Consistent with the previously reported DMP defects (Take-uchi et al. 1998, 2005), knock-down of *flr-4* or *flr-1* by RNAi increased the width of the intestinal lumen (Figures 5A-B). Remarkably, this defect was not suppressed by *twk-26(rhd182[G485E])*, which is surprising since intestinal bloating is often associated with a DR-like state (Das et al. 2023). Thus, the *twk-26(rhd182); flr-4(ut7)* and *twk-26(rhd182); flr-1(ut11)* double mutants exhibit near wild-type development and lipid accumulation yet display severe intestinal bloating. Furthermore, activation of the p38 innate immune pathway, as assessed by oligomerization of the upstream p38 regulator TIR-1/SARM1 (Peterson et al. 2022), was stimulated by

loss of *flr-4* as expected (Torzone et al. 2023); however, TIR-1 aggregation was not suppressed by the *twk-26(rhd182)* allele (Figures 5C and S6). Together, these data reveal that the DR-like state of the *flr-4* and *flr-1* mutants can be uncoupled from intestinal lumen bloating and heightened immune response, suggesting that FLR-4 and FLR-1 likely influence metabolism by coordinating intestinal nutrient absorption, which relies on ion homeostasis in the gut, rather than through an indirect mechanism.

Lastly, we explored the possibility that *twk-26(rhd182[G485E])* may suppress the abnormalities in the DMP exhibited by *flr-4* and *flr-1* mutants. The DMP is known to promote absorption of glucose in the intestine (Suzuki et al. 2022), and mutations in key DMP genes, like *flr-1*, restricts fat accumulation (Kaulich et al. 2022). Therefore, it is possible that since the *twk-26(rhd182)* allele suppressed the metabolic phenotypes of the *flr-4* and *flr-1* mutants, it may also suppress the irregular DMP of these animals; however, activation of TWK-26 did not impact the short DMP interval nor alter the number of intestinal expulsion events that were caused by the *flr* mutations (Figures 5D-E). Consistently, knock-down of *nlp-40*, which encodes an intestinal neuropeptide-like protein that controls DVB neuron activity and the expulsion step of the DMP (Wang et al. 2013), resulted in loss of P*vit-3::mCherry* reporter expression and reduced body size; however, these phenotypes were not suppressed by the *twk-26(rhd182)* allele (Figure S4). Together, these data indicate that the defects in intestinal metabolism are uncoupled from the abnormal defecation motor program in *flr* mutants and further support the notion that TWK-26 has a direct role in intestinal nutrient absorption.

DISCUSSION

In this study, we establish a role for the TWK-26 potassium channel in governing lipid homeostasis by promoting intestinal nutrient absorption in concert with the FLR-4 MAPK signaling pathway. Loss of FLR-4, or the FLR-1 sodium channel, results in slow growth, small body size, and reduced lipid accumulation, which can be attributed to impaired uptake of fatty acids and dipeptides. This defect results in a starvation-like state where the HLH-11/TFAP4 transcription factor is degraded to

initiate catabolic programs in the intestine. Remarkably, the DR-like state of the *flr-4* and *flr-1* mutants is almost completely reversed by an activating mutation in the TWK-26 potassium leak channel, which suppresses the metabolic and developmental phenotypes, but not the abnormal defecation motor program or the distended intestinal lumen phenotypes, of the *flr-4* and *flr-1* mutants. To our knowledge, this is the first example of a mutation that specifically suppresses defects in nutrient absorption, but not the DMP, in a strain that exhibits both phenotypes. Moreover, our study reveals a new mechanism by which the FLR-4 MAPK pathway and the TWK-26 potassium channel together coordinate nutrient absorption, thereby maintaining lipid homeostasis and licensing development.

Mutants in the DRL-1/FLR-4 MAPK pathway are known to exhibit DR-like phenotypes; however, the underlying cause of these phenotypes is unknown (Chamoli et al. 2014; Take-uchi et al. 2005). In genetic models of dietary restriction, it is crucial to understand the molecular mechanisms that reduce caloric intake and alter organismal physiology. The metabolic reprogramming that is conferred by loss of *drl-1*, includes increased beta-oxidation, reduced fat storage, and increased lifespan; however, the underlying cause of these phenotypes is unknown (Chamoli et al., 2014). Similarly, loss of FLR-4, which is binds DRL-1 in a protein-kinase complex (Torzone et al., 2023), promotes longevity via cytoprotective and detoxification pathways, as has also been observed in *drl-1* knock-down animals (Chamoli et al. 2014, 2020; Verma et al. 2018). Our discovery that a gain-of-function mutation in the *twk-26* potassium channel suppressed the metabolic defects of *flr-4* and *flr-1* mutants revealed, for the first time, why these mutants display strong DR phenotypes and elucidated how MAPK signaling maintains metabolic homeostasis in the intestine to promote growth and development. Moreover, our work implicates FLR-4/STK25 and FLR-1/ENaC/ASIC2 in mediating intestinal nutrient absorption, making these proteins attractive therapeutic targets in the treatment of obesity.

We demonstrate that loss of *flr-4* or *flr-1* results in a dramatic induction of autophagy in the intestine, which has been previously observed during nutrient deprivation (Chamoli et al. 2014; Hansen et al. 2008). HLH-30/TFEB is a conserved transcriptional regulator of autophagy, which when activated

promotes lysosomal biogenesis (Lapierre et al. 2013; Settembre et al. 2011). In the presence amino acids, mTORC1 is activated and phosphorylates TFEB, preventing its nuclear localization (Martina et al. 2012; Roczniak-Ferguson et al. 2012; Sparta et al. 2023). It is possible that signaling through mTORC1 is diminished in *flr-4* and *flr-1* mutants due to impaired absorption of dipeptides (Hara et al. 1998). However, upon loss of *flr-4* and *flr-1*, we observed a decrease in nuclear accumulation of HLH-30, which suggests that either mTORC1 signaling remains active or that *hlh-30*/TFEB is transcriptionally or post-translationally down-regulated in these mutants through a different mechanism. We find that HLH-11 levels are also severely decreased in the *flr* mutants. HLH-11 represses the expression of lipid catabolism genes, causing reduced intestinal lipid accumulation, and is degraded by proteosome upon starvation (Li et al. 2020). An intriguing possibility is that both HLH-30 and HLH-11 are degraded in response to impaired MAPK signaling, resulting in a nuanced transcriptional response that promotes catabolism and up-regulation of lysosomal function; however, it is unclear which transcription factor might mediate this response.

In addition to revealing the mechanism by which the FLR-4 MAPK signaling pathway maintains metabolic homeostasis, our work also establishes a new intestinal function for the TWK-26 potassium leak channel, which has not been previously characterized. KCNK3 is a mammalian ortholog of TWK-26 based on sequence similarity. In mammals, KCNK3/TASK-1 is expressed in neurons (Talley et al. 2001) and forms homodimers or heterodimers with other acid-sensitive TASK channels (Berg et al. 2004), such that these dimeric channels are activated by extracellular alkalization and inhibited by acidification. Inhibition of TASK channels like KCNK3, or its heterodimeric partner KCNK9, results in excitation of sensory neurons (Bautista et al. 2008). These acid-sensitive channels have also been described to regulate chemosensation in the carotid body, which maintains normal respiratory ventilation in mammals (Trapp et al. 2008). Thus, TASK channels, like KCNK3, play a crucial role in sensing changes in their environment to maintain homeostasis. It is intriguing that the TWK-26 potassium channel maintains metabolic homeostasis by regulating nutrient absorption, a function that has not been previously ascribed to

KCNK3. Nutrient absorption in the intestine is driven by a pH gradient across the apical membrane, where acidification of the intestinal lumen enhances the uptake of dipeptides and increases fat accumulation (Allman et al. 2009; Nehrke 2003). It is possible that the C-terminus of TWK-26, where the G485E gain-of-function mutation resides, is regulated in response to external stimuli, including nutrient availability, changes in extracellular pH, or in response to hormonal signaling. Thus, understanding the mechanism by which the G485E mutation alters channel activity will be essential to further define the role of TWK-26 in nutrient absorption.

While activation of TWK-26 promotes intestinal nutrient absorption in the absence of the FLR-4 MAPK pathway, it is surprising that it does not suppress intestinal bloating or defecation irregularities of the *flr* mutants. These phenotypes have been previously observed in DR mutants (Das et al. 2023; Katsura et al. 1994; Long et al. 2002); however, the underlying mechanism that causes bloating and constipation are unknown. mTOR pathway mutants display bloated intestinal lumens (Long et al. 2002; Meissner et al. 2004), which is further enhanced by mutation of the dipeptide transporter *pept-1* (Meissner et al. 2004), suggesting that intestinal distension may be a result of nutrient deprivation. Intestinal bloating is also observed during pathogen infection (Irazoqui et al. 2010; Singh and Aballay 2019), which upregulates an immune response and alters feeding behaviors of *C. elegans* animals. Immune signaling through p38 is hyperactive in the *drl-1* mutant, restricting growth and down-regulating vitellogenesis (Torzone et al. 2023). Consistently, we observed TIR-1 aggregation in the *flr-4(ut7)* mutant; however, hyperactivation of TWK-26 does not suppress TIR-1 puncta formation nor intestinal bloating, suggesting that restoration of ion homeostasis in the intestine promotes lipid accumulation and growth independently of altering innate immunity pathways. Additionally, activation of TWK-26 fails to suppress the defecation defects of the *flr* mutants, namely the shortened defecation interval and expulsion defects. This result is surprising, given that the DMP plays a central role in nutrient absorption, proper growth, and lipid metabolism (Kaulich et al. 2023; Suzuki et al. 2022). Our finding uniquely uncouples intestinal distension and the DMP from

metabolic homeostasis, suggesting that animals may be able to dynamically alter the expression of factors that maintain ion homeostasis to promote efficient uptake and utilization of nutrients.

The FLR-4 MAPK pathway supports growth and reproduction by promoting the absorption of fatty acids and dipeptides in the intestine. When signaling through this axis is impaired, animals fail to develop at a normal rate and exhibit a reduction in fat storage and maternal vitellogenin provisioning. Importantly, hyperactivation of the TWK-26 potassium leak channel restores intestinal homeostasis to support normal growth by increasing nutrient absorption, likely by balancing the ion gradients that govern proton-driven dipeptide transport. This work establishes a platform to investigate how MAPK pathways maintain metabolic homeostasis to promote development and enhances our understanding of how ion channels govern lipid metabolism.

METHODS

C. elegans strains

C. elegans strains were maintained on NGM media plates seeded with *E. coli* OP50 or HT115 at 20°C as previously described (Brenner 1974). Animals were synchronized at the L1 larval stage by isolating embryos via bleaching and incubating overnight in M9 buffer. All strains used in this study are listed in Supplementary Table S1.

Generation and imaging of transgenic animals

Strains carrying the high-copy *mgIs70[*P*vit-3::GFP]* or the single-copy *rhdSi42[*P*vit-3::mCherry]* transgene have been previously described (Dowen et al. 2016; Torzone et al. 2023). Strains containing *rhdSi42* were imaged using a Nikon SMZ-18 Stereo microscope with a DS-Qi2 monochrome camera.

CRISPR/Cas9 gene editing

Gene editing was conducted by germline microinjections of Cas9::crRNA::tracrRNA complexes (Integrated DNA Technologies) as previously described (Ghanta and Mello 2020). crRNA sequences are listed in Supplementary Table S2. Missense mutations were generated using single-stranded oligodeoxynucleotides as the repair donor molecule.

RNAi experiments

E. coli HT115(DE3) strains carrying the control L4440 plasmid or RNAi plasmids for knock-down of specific genes (Ahringer RNAi library) were grown for ~20 hours in Luria-Bertani media with 100 µg/mL ampicillin at 37°C. Bacteria were concentrated 30x via centrifugation and seeded onto NGM plates containing 5 mM isopropyl-β-D-thiogalactoside (IPTG) and 50 µg/ml ampicillin and were maintained overnight at room temperature to induce dsRNA expression. Synchronized L1 animals were dropped on RNAi plates and were grown to adulthood.

Oil Red O staining

Approximately 150 L4 animals were picked to new plates and harvested as day 1 adults in S-basal media. Animals were washed, fixed with 60% isopropanol, and stained for 7 hours with 0.5% Oil Red O as previously described (Dowen 2019). Animals were mounted on 2% agarose pads and imaged using a Nikon SMZ-18 Stereo microscope equipped with a DS-Qi2 monochrome camera for intensity analyses and a Nikon Ti2 widefield microscope equipped with a DS-Fi3 camera for representative color images. Quantification of Oil Red O staining was conducted by manually outlining worms in ImageJ (Schindelin et al. 2012) and then measuring the mean gray value within the area of each worm. These values were subtracted from the maximum gray value for 16-bit images, 65,526, as previously described (DuMez-Kornegay et al. 2024). Data were plotted and analyzed using Prism 9. A one-way ANOVA with a Bonferroni correction was used to calculate *P* values.

Nile Red staining

A Nile Red stock solution was prepared in acetone at 0.5 mg/mL and stored at 4°C. Approximately 150 L4 animals were picked to new plates and harvested 24 hours later as day 1 adults in S-basal media. Animals were washed, fixed in 60% isopropanol, and stained for 2 hours in 0.03 mg/mL Nile Red. Animals were mounted on 2% agarose pads and imaged with a Nikon Ti2 widefield microscope equipped with a Hamamatsu ORCA-Fusion BT camera. Quantification of fluorescent intensity was conducted by manually outlining worms in Fiji and measuring the average intensity within the area of each animal. Values were plotted and statistical analyses were performed using Prism 9. A one-way ANOVA was conducted with Bonferroni corrections to calculate *P* values.

Growth and body size assays

For developmental growth rate assays, animals were grown on their respective food sources for several generations without starvation prior to being assayed. Approximately 100-200 eggs were picked from plates containing freshly-laid embryos (20 hours or less) to new plates and scored every 24 hours for 7 days. Gravid adults were removed from the population and recorded as having reached adulthood. For the single time point developmental assays (Figure 2), animals were grown from synchronized L1s and the developmental stage for each worm was recorded at the indicated time point across the entire population.

To quantify body size, animals were grown similarly, picked from plates at the L4 larval stage, transferred to new plates seeded with their respective food source, and maintained for 24 hours prior to being imaged. Day 1 adult animals were mounted on 2% agarose pads with levamisole and imaged with a Nikon SMZ-18 stereo microscope equipped with a DS-Qi2 monochrome camera. Using the Fiji software, body size measurements were obtained by manually outlining individual worms and obtaining an area in pixels, which was later converted to mm^2 according to the known imaging parameters. Body size data were plotted and statistical analysis (one-way ANOVA with a Bonferroni correction for multiple testing) was performed in Prism 9.

Quantitative PCR

Preparation of total RNA and qPCR assays were performed exactly as previously described (Torzone et al. 2023). All primer sequences are listed in Supplementary Table S3.

EMS Mutagenesis

Mutagenesis of *flr-4(ut7); mgIs70* animals was performed using ethyl methanesulfonate (EMS, Sigma-Aldrich) and was conducted as previously described (Dowen et al. 2016). Approximately 150,000 haploid genomes were screened and suppressor mutants were selected in the F1 generation based on normal growth rate and increased *mgIs70[vit-3::GFP]* expression relative to the non-mutagenized *flr-4(ut7); mgIs70* strain. Suppressor strains were backcrossed to the parental strain four times, the genomic DNA was isolated using the Qiagen Gentra Puregene Tissue Kit (Doitsidou et al. 2010), and libraries for whole genome sequencing were prepared and sequenced by Novogene (Sacramento, CA) using an Illumina NovaSeq instrument (PE 150). Candidate suppressor mutations were identified using in-house scripts, as previously described (Minevich et al. 2012).

Reporter imaging and quantification

P*vit-3::mCherry* fluorescence was measured in strains containing the *rhdSi42* reporter. Animals were grown until the L4 stage, picked to new plates, and imaged 24 hours later as day 1 adults on a 2% agarose pad containing levamisole. A Nikon SMZ-18 Stereo microscope equipped with a DS-Qi2 monochrome camera was used for imaging. In Fiji, the body of each animal was manually outlined in the bright field channel and the mean intensity values were obtained in the mCherry channel. The values were plotted in Prism 9 and a one-way ANOVA with a Bonferroni correction for multiple testing was conducted to obtain *P* values.

To image the HLH-30::GFP and HLH-11::GFP transcription factors, strains containing the *sqIs19[HLH-30::GFP]* or *wgIs396[HLH-11::TY1::EGFP::3xFLAG]* transgenes were grown on RNAi plates until the L4 stage, picked to fresh RNAi plates, and imaged 24 hours later as day 1 adults on 2% agarose pads containing levamisole using a Nikon Ti2 widefield microscope equipped with a Hamamatsu ORCA-Fusion BT camera. A 10x objective was used to capture representative images.

The *sqIs11[mCherry::GFP::LGG-1]* reporter was used to measure autophagic lysosomes (Chang et al. 2017). Imaging was conducted using a CFI Apo 60X Oil TIRF objective on a Nikon Ti2 widefield microscope equipped with a Hamamatsu ORCA-Fusion BT camera. Animals were grown to the L4 stage on RNAi plates and transferred to freshly made RNAi plates 24 hours prior to imaging. Day 1 adult animals were mounted on 2% agarose pads with levamisole and the posterior-most intestinal cells were imaged in the bright field, mCherry, and FITC channels. Autophagic lysosomes were measured in the posterior intestine where the last 2-4 cells are unobstructed by other tissues. Z-stacks were cropped to 0.6 μm to capture planes of the intestine that were easily visualized. Z-stacks were then denoised, deconvoluted, and compressed into a single image using the Nikon NIS-Elements analysis software. Hand-drawn ROIs were placed around the 2-4 posterior-most intestinal cells and mCherry puncta were quantified using the object counts feature in NIS-elements. Counts of LGG-1::mCherry puncta and the puncta area relative to the ROI area were plotted in Prism 9 and a one-way ANOVA with a Bonferroni correction was performed to calculate *P* values.

To measure intestinal lumen widths, the *erm-1(mib15[erm-1::eGFP])* strain was used to mark the intestinal lumen (Ramalho et al. 2020). Animals were grown on RNAi plates, picked at the L4 larval stage to fresh RNAi plates, and imaged 24 hours later as day 1 adults mounted on 2% agarose pads containing levamisole. The Nikon Ti2 widefield microscope equipped with a Hamamatsu ORCA-Fusion BT camera was used to image animals at 20x. Intestinal lumen widths were measured in the middle of the animal where the intestine was not obstructed by other tissues. Lumen widths from 30 animals were obtained and

plotted in Prism 9 and a one-way ANOVA with a Bonferroni correction was performed to calculate *P* values.

Nutrient absorption assays

For *ad libitum* feeding, a 10 mM stock solution of C1-BODIPY-C12 (Thermo Fisher) was diluted in S-basal media and overlaid onto bacterial lawns for a final concentration of 10 μM in the NGM plate (Mak et al. 2006; O'Rourke et al. 2009). Plates were allowed to dry for one hour prior to picking day 1 adults to BODIPY plates. Worms were fed BODIPY *ad libitum* for 2 hours and subsequently mounted onto 2% agarose pads containing levamisole for imaging with a 20x objective on a Nikon Ti2 widefield microscope equipped with a Hamamatsu ORCA-Fusion BT camera. All plates or eppendorf tubes containing BODIPY were covered with aluminum foil to protect the reagent from light.

Nile Red feeding was performed as previously described (Mak et al. 2006) with the following modifications: eggs or L1s were picked to Nile Red-containing plates and animals were imaged as day 1 adults. Animals were mounted on 2% agarose pads containing levamisole and imaged using a Nikon SMZ-18 Stereo microscope with a DS-Qi2 monochrome camera. All plates containing Nile Red were covered with aluminum foil to protect from light.

For dipeptide absorption assays, feeding with β-Ala-Lys-AMCA (BioSynth) was performed as previously described (Meissner et al. 2004). Briefly, animals were grown until the L4 stage, picked to fresh *E. coli* OP50-seeded NGM plates, grown for 24 hours, and transferred to 0.5 mL Eppendorf tubes containing 1 mM β-Ala-Lys-AMCA in 100 μL of M9 media. The samples were covered in aluminum foil, incubated for 3 hours with gentle rocking, washed three times with M9, and mounted on 2% agarose pads containing levamisole for imaging with a Nikon Ti2 widefield microscope equipped with a Hamamatsu ORCA-Fusion BT camera.

Defecation assays

Videos of day 1 adult animals were recorded using a Nikon SMZ-18 Stereo microscope with a DS-Qi2 monochrome camera. Animals were permitted to freely move and feed on *E. coli* OP50 NGM plates and one animal at a time was recorded for a total of 5 complete defecation cycles, each one marked by a posterior body wall contraction (pBoc) (Iwasaki et al. 1995; Liu and Thomas 1994). The time interval between pBoc events was recorded as the DMP interval, and the number of expulsion (exp) events observed during the 5 recorded defecation cycles were noted. Animals were removed from the plate after recording to ensure that 10 unique individuals were assayed per strain. Data were plotted in Prism 9 and a one-way ANOVA was performed with a Bonferroni correction for multiple testing to calculate *P* values.

AUTHOR CONTRIBUTIONS

S.K.T. and R.H.D. designed the experiments. S.K.T., P.C.B., N.R.C., and K.N.S. performed the experiments. S.K.T, K.N.S, and R.H.D interpreted the results. S.K.T prepared the original draft of the manuscript. S.K.T and R.H.D reviewed and edited the manuscript. R.H.D secured funding for the study.

FUNDING

This study was supported by the National Institute of General Medical Sciences grant R35GM137985 to R.H.D.

ACKNOWLEDGEMENTS

The Caenorhabditis Genetics Center provided some of the strains used in this study, which is supported by the NIH Office of Research Infrastructure Programs (P40 OD010440). We would like to thank Dr. Laura Huff for technical assistance in our BODIPY staining experiments.

CONFLICT OF INTEREST

The authors declare no competing interests.

REFERENCES

Al-Hazza A, Linley JE, Aziz Q, MacLennan KA, Hunter M, Sandle GI. 2012. Potential role of reduced basolateral potassium (IKCa3.1) channel expression in the pathogenesis of diarrhoea in ulcerative colitis. *J Pathol* **226**: 463–470.

Allman E, Johnson D, Nehrke K. 2009. Loss of the apical V-ATPase a-subunit VHA-6 prevents acidification of the intestinal lumen during a rhythmic behavior in *C. elegans*. *Am J Physiol-Cell Physiol* **297**: C1071–C1081.

Amrutkar M, Kern M, Nuñez-Durán E, Ståhlman M, Cansby E, Chursa U, Stenfeldt E, Borén J, Blüher M, Mahlapuu M. 2016. Protein kinase STK25 controls lipid partitioning in hepatocytes and correlates with liver fat content in humans. *Diabetologia* **59**: 341–353.

Anderson KJ, Cormier RT, Scott PM. 2019. Role of ion channels in gastrointestinal cancer. *World J Gastroenterol* **25**: 5732–5772.

Bautista DM, Sigal YM, Milstein AD, Garrison JL, Zorn JA, Tsuruda PR, Nicoll RA, Julius D. 2008. Pungent agents from Szechuan peppers excite sensory neurons by inhibiting two-pore potassium channels. *Nat Neurosci* **11**: 772–779.

Berg AP, Talley EM, Manger JP, Bayliss DA. 2004. Motoneurons express heteromeric TWIK-related acid-sensitive K+ (TASK) channels containing TASK-1 (KCNK3) and TASK-3 (KCNK9) subunits. *J Neurosci Off J Soc Neurosci* **24**: 6693–6702.

Branicky R, Hekimi S. 2006. What keeps C. elegans regular: the genetics of defecation. *Trends Genet* **22**: 571–579.

Brenner S. 1974. The genetics of Caenorhabditis elegans. *Genetics* **77**: 71–94.

Chamoli M, Goyala A, Tabrez SS, Siddiqui AA, Singh A, Antebi A, Lithgow GJ, Watts JL, Mukhopadhyay A. 2020. Polyunsaturated fatty acids and p38-MAPK link metabolic reprogramming to cytoprotective gene expression during dietary restriction. *Nat Commun* **11**: 4865.

Chamoli M, Singh A, Malik Y, Mukhopadhyay A. 2014. A novel kinase regulates dietary restriction-mediated longevity in Caenorhabditis elegans. *Aging Cell* **13**: 641–655.

Chang JT, Kumsta C, Hellman AB, Adams LM, Hansen M. 2017. Spatiotemporal regulation of autophagy during Caenorhabditis elegans aging. *eLife* **6**: e18459.

Das P, Aballay A, Singh J. 2023. Calcineurin inhibition enhances Caenorhabditis elegans lifespan by defecation defects-mediated calorie restriction and nuclear hormone signaling. https://elifesciences.org/reviewed-preprints/89572v1 (Accessed May 1, 2024).

Doitsidou M, Poole RJ, Sarin S, Bigelow H, Hobert O. 2010. C. elegans Mutant Identification with a One-Step Whole-Genome-Sequencing and SNP Mapping Strategy ed. A.C. Hart. *PLoS ONE* **5**: e15435.

Dowen RH. 2019. CEH-60/PBX and UNC-62/MEIS Coordinate a Metabolic Switch that Supports Reproduction in C. elegans. *Dev Cell* **49**: 235-250.e7.

Dowen RH, Breen PC, Tullius T, Conery AL, Ruvkun G. 2016. A microRNA program in the *C. elegans* hypodermis couples to intestinal mTORC2/PQM-1 signaling to modulate fat transport. *Genes Dev* **30**: 1515–1528.

DuMez-Kornegay RN, Baker LS, Morris AJ, DeLoach WLM, Dowen RH. 2024. Kombucha Tea-associated microbes remodel host metabolic pathways to suppress lipid accumulation. *PLoS Genet* **20**: e1011003.

Duprat F, Lesage F, Fink M, Reyes R, Heurteaux C, Lazdunski M. 1997. TASK, a human background K+ channel to sense external pH variations near physiological pH. *EMBO J* **16**: 5464–5471.

Feliciangeli S, Chatelain FC, Bichet D, Lesage F. 2015. The family of K2P channels: salient structural and functional properties. *J Physiol* **593**: 2587–2603.

Ghanta KS, Mello CC. 2020. Melting dsDNA Donor Molecules Greatly Improves Precision Genome Editing in Caenorhabditis elegans. *Genetics* **216**: 643–650.

Gottschling D-C, Döring F, Lüersen K. 2017. Locomotion Behavior Is Affected by the GαS Pathway and the Two-Pore-Domain K+ Channel TWK-7 Interacting in GABAergic Motor Neurons in Caenorhabditis elegans. *Genetics* **206**: 283–297.

Gruss M, Corsi AK. 2022. Using Caenorhabditis elegans as a Model for Mechanistic Insights of Craniofacial Development. *Methods Mol Biol Clifton NJ* **2403**: 1–18.

Hansen M, Chandra A, Mitic LL, Onken B, Driscoll M, Kenyon C. 2008. A role for autophagy in the extension of lifespan by dietary restriction in C. elegans. *PLoS Genet* **4**: e24.

Hara K, Yonezawa K, Weng QP, Kozlowski MT, Belham C, Avruch J. 1998. Amino acid sufficiency and mTOR regulate p70 S6 kinase and eIF-4E BP1 through a common effector mechanism. *J Biol Chem* **273**: 14484–14494.

Hobert O. 2013. The neuronal genome of Caenorhabditis elegans. *WormBook Online Rev C Elegans Biol* 1–106.

Honey KL, Torzone SK, Dowen RH. 2023. The C. elegansflr-3(ut9) mutation is a loss-of-function insertion within the drl-1 locus. *MicroPublication Biol* **2023**.

Irazoqui JE, Troemel ER, Feinbaum RL, Luhachack LG, Cezairliyan BO, Ausubel FM. 2010. Distinct pathogenesis and host responses during infection of C. elegans by P. aeruginosa and S. aureus. *PLoS Pathog* **6**: e1000982.

Iwasaki K, Liu DW, Thomas JH. 1995. Genes that control a temperature-compensated ultradian clock in Caenorhabditis elegans. *Proc Natl Acad Sci U S A* **92**: 10317–10321.

Katsura I, Kondo K, Amano T, Ishihara T, Kawakami M. 1994. Isolation, characterization and epistasis of fluoride-resistant mutants of Caenorhabditis elegans. *Genetics* **136**: 145–154.

Kaulich E, Carroll T, Ackley BD, Tang Y-Q, Hardege I, Nehrke K, Schafer WR, Walker DS. 2022. Distinct roles for two Caenorhabditis elegans acid-sensing ion channels in an ultradian clock. *eLife* **11**: e75837.

Kaulich E, Grundy LJ, Schafer WR, Walker DS. 2023. The diverse functions of the DEG/ENaC family: linking genetic and physiological insights. *J Physiol* **601**: 1521–1542.

Kimble J, Sharrock WJ. 1983. Tissue-specific synthesis of yolk proteins in Caenorhabditis elegans. *Dev Biol* **96**: 189–196.

Kobayashi Y, Kimura KD, Katsura I. 2011. Ultradian rhythm in the intestine of Caenorhabditis elegans is controlled by the C-terminal region of the FLR-1 ion channel and the hydrophobic domain of the FLR-4 protein kinase: Ultradian clock regulated by ion channel. *Genes Cells* **16**: 565–575.

Lapierre LR, De Magalhaes Filho CD, McQuary PR, Chu C-C, Visvikis O, Chang JT, Gelino S, Ong B, Davis AE, Irazoqui JE, et al. 2013. The TFEB orthologue HLH-30 regulates autophagy and modulates longevity in Caenorhabditis elegans. *Nat Commun* **4**: 2267.

Li Y, Ding W, Li C-Y, Liu Y. 2020. HLH-11 modulates lipid metabolism in response to nutrient availability. *Nat Commun* **11**: 5959.

Lin-Moore AT, Oyeyemi MJ, Hammarlund M. 2021. rab-27 acts in an intestinal pathway to inhibit axon regeneration in C. elegans ed. G.P. Copenhaver. *PLOS Genet* **17**: e1009877.

Liu DW, Thomas JH. 1994. Regulation of a periodic motor program in C. elegans. *J Neurosci Off J Soc Neurosci* **14**: 1953–1962.

Long X, Spycher C, Han ZS, Rose AM, Müller F, Avruch J. 2002. TOR Deficiency in C. elegans Causes Developmental Arrest and Intestinal Atrophy by Inhibition of mRNA Translation. *Curr Biol* **12**: 1448–1461.

Lu X, Luo C, Wu J, Deng Y, Mu X, Zhang T, Yang X, Liu Q, Li Z, Tang S, et al. 2023. Ion channels and transporters regulate nutrient absorption in health and disease. *J Cell Mol Med* **27**: 2631–2642.

Magalhães D, Cabral JM, Soares-da-Silva P, Magro F. 2016. Role of epithelial ion transports in inflammatory bowel disease. *Am J Physiol Gastrointest Liver Physiol* **310**: G460-476.

Mak HY, Nelson LS, Basson M, Johnson CD, Ruvkun G. 2006. Polygenic control of Caenorhabditis elegans fat storage. *Nat Genet* **38**: 363–368.

Martina JA, Chen Y, Gucek M, Puertollano R. 2012. MTORC1 functions as a transcriptional regulator of autophagy by preventing nuclear transport of TFEB. *Autophagy* **8**: 903–914.

Meissner B, Boll M, Daniel H, Baumeister R. 2004. Deletion of the Intestinal Peptide Transporter Affects Insulin and TOR Signaling in Caenorhabditis elegans. *J Biol Chem* **279**: 36739–36745.

Minevich G, Park DS, Blankenberg D, Poole RJ, Hobert O. 2012. CloudMap: A Cloud-Based Pipeline for Analysis of Mutant Genome Sequences. *Genetics* **192**: 1249–1269.

Nehrke K. 2003. A Reduction in Intestinal Cell pH Due to Loss of the Caenorhabditis elegans Na+/H+ Exchanger NHX-2 Increases Life Span. *J Biol Chem* **278**: 44657–44666.

Oishi A, Gengyo-Ando K, Mitani S, Mohri-Shiomi A, Kimura KD, Ishihara T, Katsura I. 2009. FLR-2, the glycoprotein hormone alpha subunit, is involved in the neural control of intestinal functions in *Caenorhabditis elegans*. *Genes Cells* **14**: 1141–1154.

O'Rourke EJ, Ruvkun G. 2013. MXL-3 and HLH-30 transcriptionally link lipolysis and autophagy to nutrient availability. *Nat Cell Biol* **15**: 668–676.

O'Rourke EJ, Soukas AA, Carr CE, Ruvkun G. 2009. C. elegans Major Fats Are Stored in Vesicles Distinct from Lysosome-Related Organelles. *Cell Metab* **10**: 430–435.

Peterson ND, Icso JD, Salisbury JE, Rodríguez T, Thompson PR, Pukkila-Worley R. 2022. Pathogen infection and cholesterol deficiency activate the C. elegans p38 immune pathway through a TIR-1/SARM1 phase transition. *eLife* **11**: e74206.

Pfeiffer J, Johnson D, Nehrke K. 2008. Oscillatory Transepithelial H+ Flux Regulates a Rhythmic Behavior in C. elegans. *Curr Biol* **18**: 297–302.

Ramalho JJ, Sepers JJ, Nicolle O, Schmidt R, Cravo J, Michaux G, Boxem M. 2020. C-terminal phosphorylation modulates ERM-1 localization and dynamics to control cortical actin organization and support lumen formation during *C. elegans* development. *Development* dev.188011.

Roczniak-Ferguson A, Petit CS, Froehlich F, Qian S, Ky J, Angarola B, Walther TC, Ferguson SM. 2012. The transcription factor TFEB links mTORC1 signaling to transcriptional control of lysosome homeostasis. *Sci Signal* **5**: ra42.

Rödström KEJ, Kiper AK, Zhang W, Rinné S, Pike ACW, Goldstein M, Conrad LJ, Delbeck M, Hahn MG, Meier H, et al. 2020. A lower X-gate in TASK channels traps inhibitors within the vestibule. *Nature* **582**: 443–447.

Schindelin J, Arganda-Carreras I, Frise E, Kaynig V, Longair M, Pietzsch T, Preibisch S, Rueden C, Saalfeld S, Schmid B, et al. 2012. Fiji: an open-source platform for biological-image analysis. *Nat Methods* **9**: 676–682.

Settembre C, De Cegli R, Mansueto G, Saha PK, Vetrini F, Visvikis O, Huynh T, Carissimo A, Palmer D, Klisch TJ, et al. 2013. TFEB controls cellular lipid metabolism through a starvation-induced autoregulatory loop. *Nat Cell Biol* **15**: 647–658.

Settembre C, Di Malta C, Polito VA, Garcia Arencibia M, Vetrini F, Erdin S, Erdin SU, Huynh T, Medina D, Colella P, et al. 2011. TFEB links autophagy to lysosomal biogenesis. *Science* **332**: 1429–1433.

Sheng M, Hosseinzadeh A, Muralidharan SV, Gaur R, Selstam E, Tuck S. 2015. Aberrant Fat Metabolism in Caenorhabditis elegans Mutants with Defects in the Defecation Motor Program ed. A.C. Hart. *PLOS ONE* **10**: e0124515.

Singh J, Aballay A. 2019. Microbial Colonization Activates an Immune Fight-and-Flight Response via Neuroendocrine Signaling. *Dev Cell* **49**: 89-99.e4.

Singh R, Kaushik S, Wang Y, Xiang Y, Novak I, Komatsu M, Tanaka K, Cuervo AM, Czaja MJ. 2009. Autophagy regulates lipid metabolism. *Nature* **458**: 1131–1135.

Sörmann J, Schewe M, Proks P, Jouen-Tachoire T, Rao S, Riel EB, Agre KE, Begtrup A, Dean J, Descartes M, et al. 2022. Gain-of-function mutations in KCNK3 cause a developmental disorder with sleep apnea. *Nat Genet* **54**: 1534–1543.

Spanier B, Lasch K, Marsch S, Benner J, Liao W, Hu H, Kienberger H, Eisenreich W, Daniel H. 2009. How the Intestinal Peptide Transporter PEPT-1 Contributes to an Obesity Phenotype in Caenorhabditits elegans ed. I.A. Hansen. *PLoS ONE* **4**: e6279.

Sparta B, Kosaisawe N, Pargett M, Patankar M, DeCuzzi N, Albeck JG. 2023. Continuous sensing of nutrients and growth factors by the mTORC1-TFEB axis eds. I. Topisirovic, D.E. James, and I. Topisirovic. *eLife* **12**: e74903.

Suzuki Y, Kikuchi K, Numayama-Tsuruta K, Ishikawa T. 2022. Reciprocating intestinal flows enhance glucose uptake in C. elegans. *Sci Rep* **12**: 15310.

Take-uchi M, Kawakami M, Ishihara T, Amano T, Kondo K, Katsura I. 1998. An ion channel of the degenerin/epithelial sodium channel superfamily controls the defecation rhythm in *Caenorhabditis elegans*. *Proc Natl Acad Sci* **95**: 11775–11780.

Take-uchi M, Kobayashi Y, Kimura KD, Ishihara T, Katsura I. 2005. FLR-4, a Novel Serine/Threonine Protein Kinase, Regulates Defecation Rhythm in *Caenorhabditis elegans*. *Mol Biol Cell* **16**: 1355–1365.

Talley EM, Solorzano G, Lei Q, Kim D, Bayliss DA. 2001. Cns distribution of members of the two-pore-domain (KCNK) potassium channel family. *J Neurosci Off J Soc Neurosci* **21**: 7491–7505.

Tan KT, Luo S-C, Ho W-Z, Lee Y-H. 2011. Insulin/IGF-1 receptor signaling enhances biosynthetic activity and fat mobilization in the initial phase of starvation in adult male C. elegans. *Cell Metab* **14**: 390–402.

Thomas JH. 1990. Genetic analysis of defecation in Caenorhabditis elegans. *Genetics* **124**: 855–872.

Thwaites DT, Ford D, Glanville M, Simmons NL. 1999. H(+)/solute-induced intracellular acidification leads to selective activation of apical Na(+)/H(+) exchange in human intestinal epithelial cells. *J Clin Invest* **104**: 629–635.

Thwaites DT, Kennedy DJ, Raldua D, Anderson CMH, Mendoza ME, Bladen CL, Simmons NL. 2002. H+/dipeptide absorption across the human intestinal epithelium is controlled indirectly via a functional Na+/H+ exchanger. *Gastroenterology* **122**: 1322–1333.

Torzone SK, Park AY, Breen PC, Cohen NR, Dowen RH. 2023. Opposing action of the FLR-2 glycoprotein hormone and DRL-1/FLR-4 MAP kinases balance p38-mediated growth and lipid homeostasis in C. elegans ed. A.P. Gould. *PLOS Biol* **21**: e3002320.

Trapp S, Isabel Aller M, Wisden W, Gourine AV. 2008. A Role for TASK-1 (KCNK3) Channels in the Chemosensory Control of Breathing. *J Neurosci* **28**: 8844–8850.

Tsirigos KD, Peters C, Shu N, Käll L, Elofsson A. 2015. The TOPCONS web server for consensus prediction of membrane protein topology and signal peptides. *Nucleic Acids Res* **43**: W401-407.

Verma S, Jagtap U, Goyala A, Mukhopadhyay A. 2018. A novel gene-diet pair modulates C. elegans aging ed. S.S. Lee. *PLOS Genet* **14**: e1007608.

Wang H, Girskis K, Janssen T, Chan JP, Dasgupta K, Knowles JA, Schoofs L, Sieburth D. 2013. Neuropeptide Secreted from a Pacemaker Activates Neurons to Control a Rhythmic Behavior. *Curr Biol CB* **23**: 746–754.

Yue Z, Li Y, Yu B, Xu Y, Chen L, Chitturi J, Meng J, Hung W, Tian Y, Mouridi SE, et al. 2022. A Leak K^+ Channel TWK-40 Regulates Rhythmic Motor Program in *C. elegans*. http://biorxiv.org/lookup/doi/10.1101/2022.04.09.487752 (Accessed April 18, 2024).

Zhang Y, Xu J, Qiu Z, Guan Y, Zhang X, Zhang X, Chai D, Chen C, Hu Q, Wang W. 2022. STK25 enhances hepatocellular carcinoma progression through the STRN/AMPK/ACC1 pathway. *Cancer Cell Int* **22**: 4.

Zhou C, Zhou Q, He X, He Y, Wang X, Zhu X, Zhang Y, Ma L. 2022. Differential modulation of C. elegans motor behavior by NALCN and two-pore domain potassium channels ed. A.C. Hart. *PLOS Genet* **18**: e1010126.

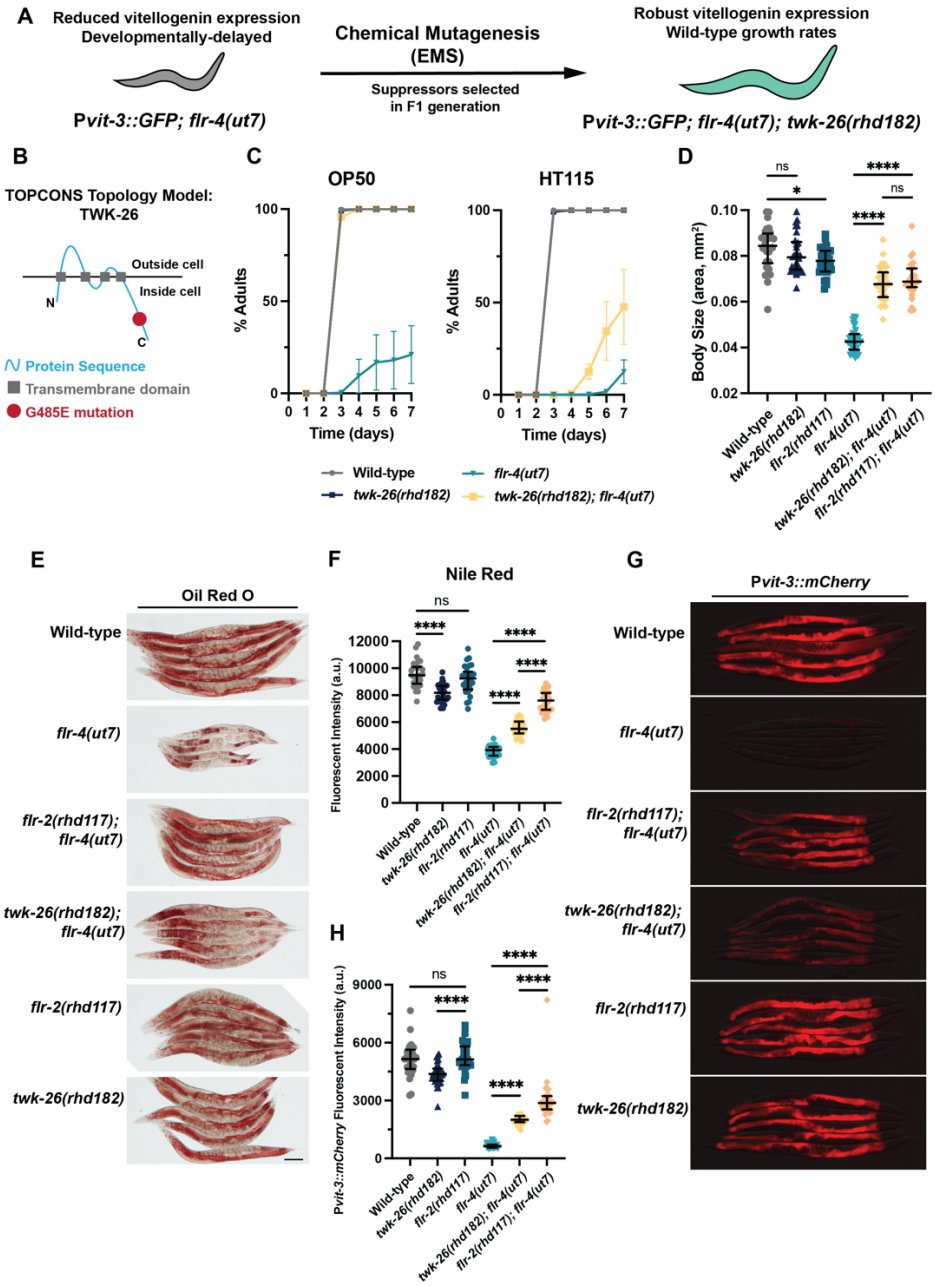

Figure 1. A *twk-26* mutation suppresses the growth and lipid metabolism defects exhibited by the *flr-4* mutant, (A) A diagram illustrating the design of the EMS mutagenesis screen using the *mgIs70[*P*vit-3::GFP]* vitellogenesis reporter. Mutations that suppressed the slow growth and defects in reporter expression of the *flr-4(ut7)* mutant were selected in the F1 generation, thereby enriching for gain-of-function mutations. (B) A transmembrane topology prediction of TWK-26 based on amino acid sequence. The *twk-26(rhd182[G485E])* mutation resides in the C-terminal tail. (C) Growth rate of the indicated strains consuming either *E. coli* OP50 or HT115. Data are presented as the mean +/− SEM of 3 independent experiments. (D) Body size of the indicated strains at day 1 of adulthood. Data are presented as the median and interquartile range (ns, not significant, *, $P<0.05$, ****, $P<0.0001$, one-way ANOVA). (E) Representative images of the indicated strains stained with Oil Red O (day 1 adults; scale bar, 100 µm). (F) Quantification of Nile Red staining of the indicated strains as day 1 adults (median and interquartile range; ns, not significant, ****, $P<0.0001$, one-way ANOVA). (G) Representative overlaid DIC and mCherry fluorescence images and (H) quantification of P*vit-3::mCherry* expression (median and interquartile range; ns, not significant, ****, $P<0.0001$, one-way ANOVA) for the indicated strains at day 1 of adulthood. (C-H) All strains contain the *rhdSi42[*P*vit-3::mCherry]* transgene.

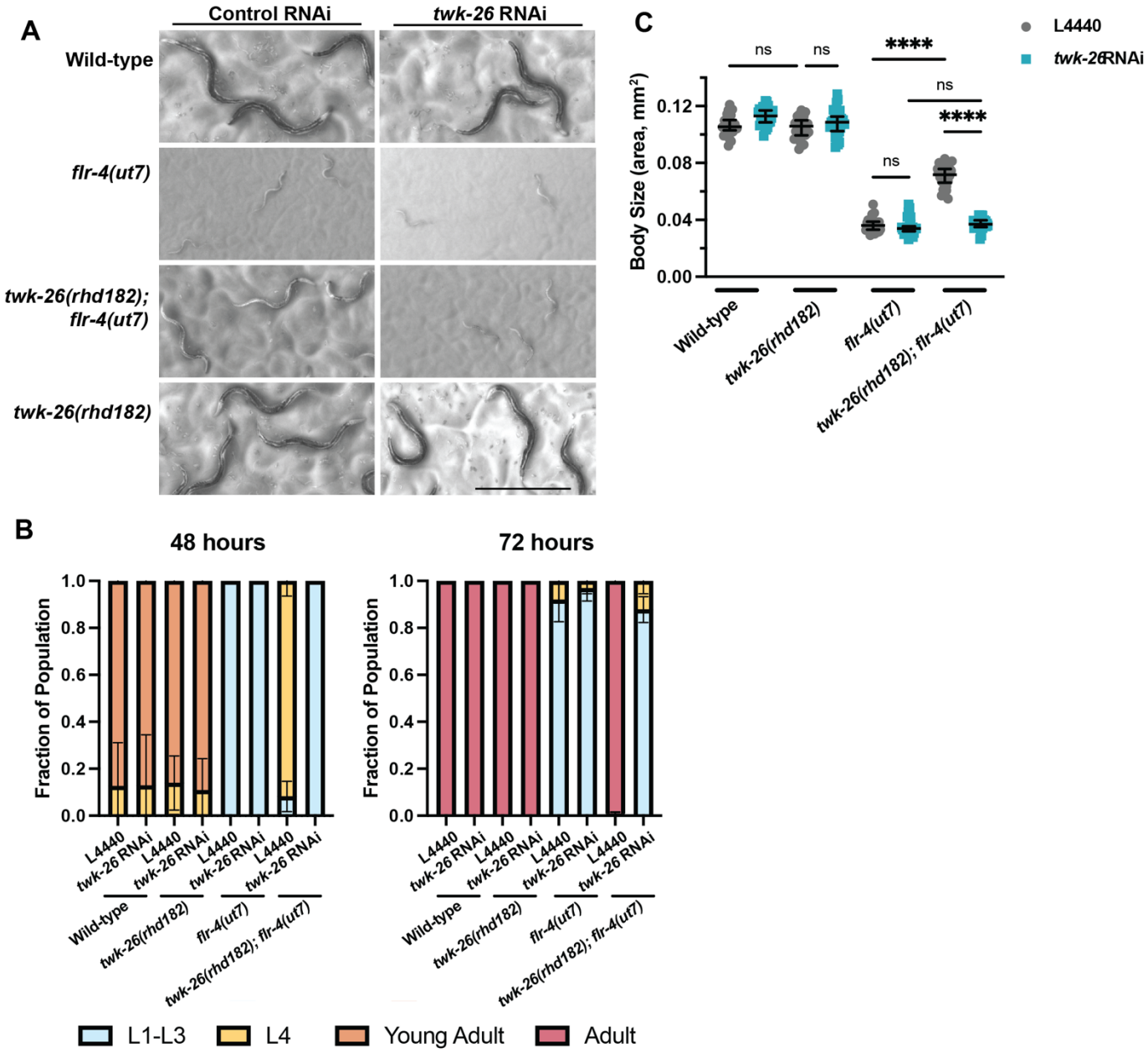

Figure 2. Activation of *twk-26* suppresses *flr-4* metabolic deficiencies. (A) Representative bright field images of the indicated strains subjected to control or *twk-26* RNAi for 72 hours (scale bar, 500 µm). (B) Fraction of the population at each developmental stage (mean +/- SD) after treatment of the indicated strains with control or *twk-26* RNAi for 48 or 72 hours. (C) Body size of the indicated strains (day 1 adults; median and interquartile range; ns, not significant, ****, $P<0.0001$, one-way ANOVA). (A-C) All strains contain the P*vit-3::mCherry* reporter.

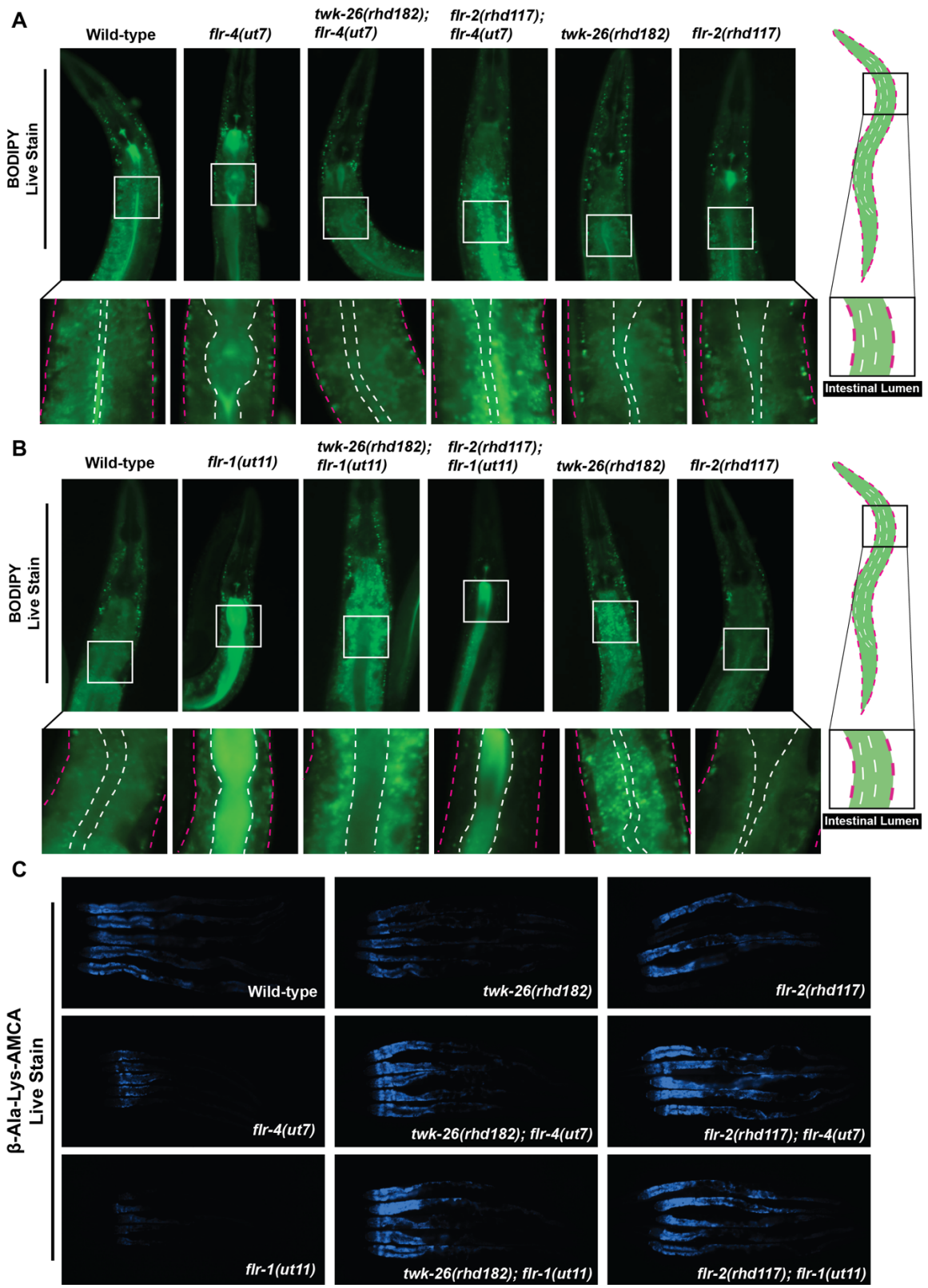

Figure 3. TWK-26 restores nutrient absorption in the intestine of *flr-4* and *flr-1* mutants. (A-B) Representative fluorescence images of the anterior intestine of day 1 adult animals after 2 hours of *ad libitum* C1-BODIPY-C12 feeding for the indicated strains. Intestinal lumens are outlined in white and the exterior of each animal is outlined in pink. (C) Representative fluorescence images of day 1 adult animals incubated for 3 hours in 1 mM β-Ala-Lys-AMCA, a fluorescently labeled dipeptide (5 animals per image).

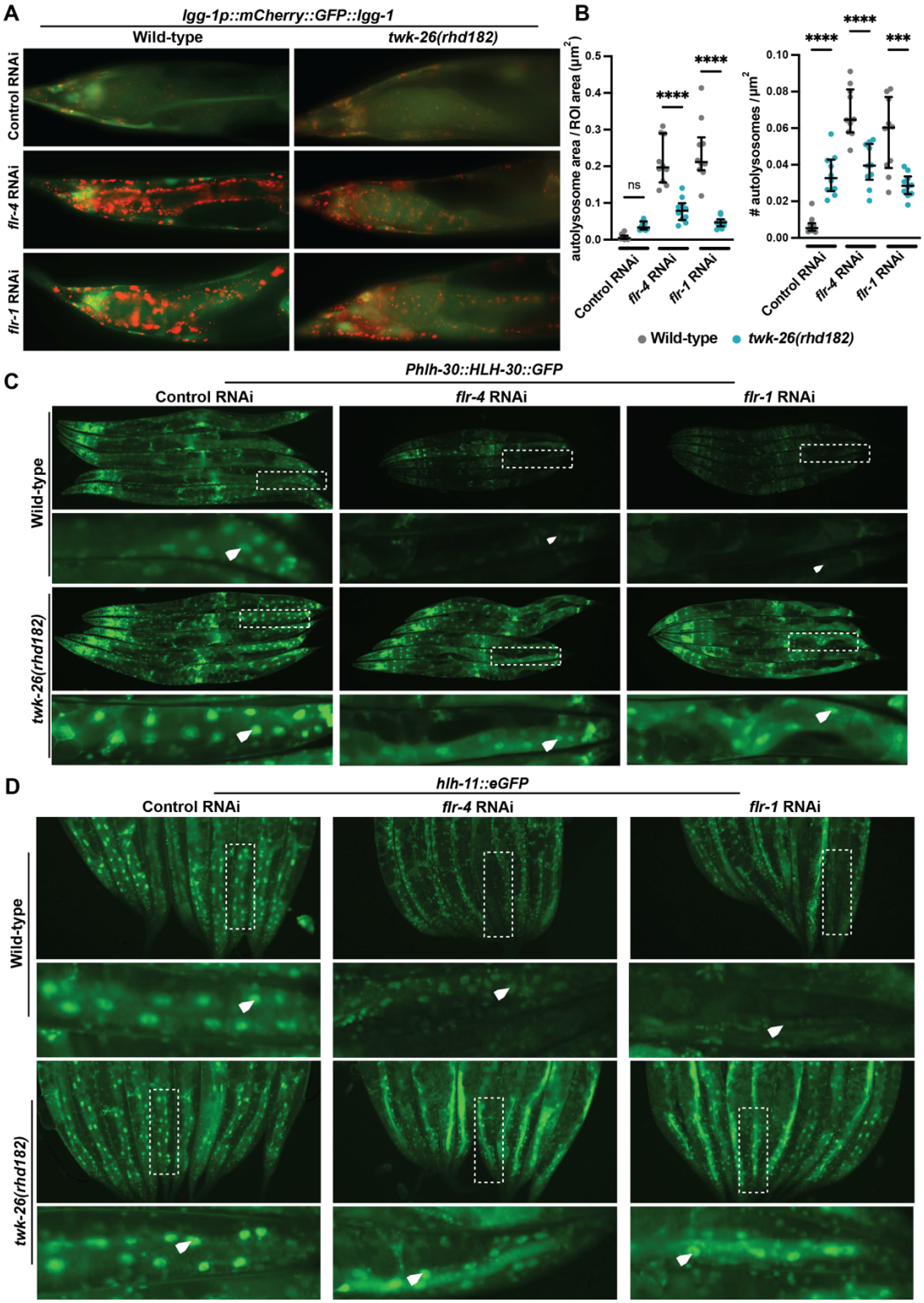

Figure 4. TWK-26 suppresses autophagy in the *flr-4* and *flr-1* mutants through HLH-11. (A) Representative images of mCherry::GFP::LGG-1 puncta in posterior intestinal cells of wild-type or *twk-26(rhd182)* day 1 adult animals subjected to control, *flr-4*, or *flr-1* RNAi. Autolysosomes are labelled by mCherry alone since the GFP signal is quenched. (B) Quantification of the area (left) and the total number (right) of autolysosomes in the posterior intestine. Data are presented as median and interquartile range (ns, not significant, ***, P=0.0001, ****, P<0.0001, one-way ANOVA). Representative fluorescence images of (C) HLH-30::GFP or (D) HLH-11::GFP in wild-type or *twk-26(rhd182)* day 1 adult animals following control, *flr-4*, or *flr-1* RNAi. White arrowheads indicate intestinal nuclei.

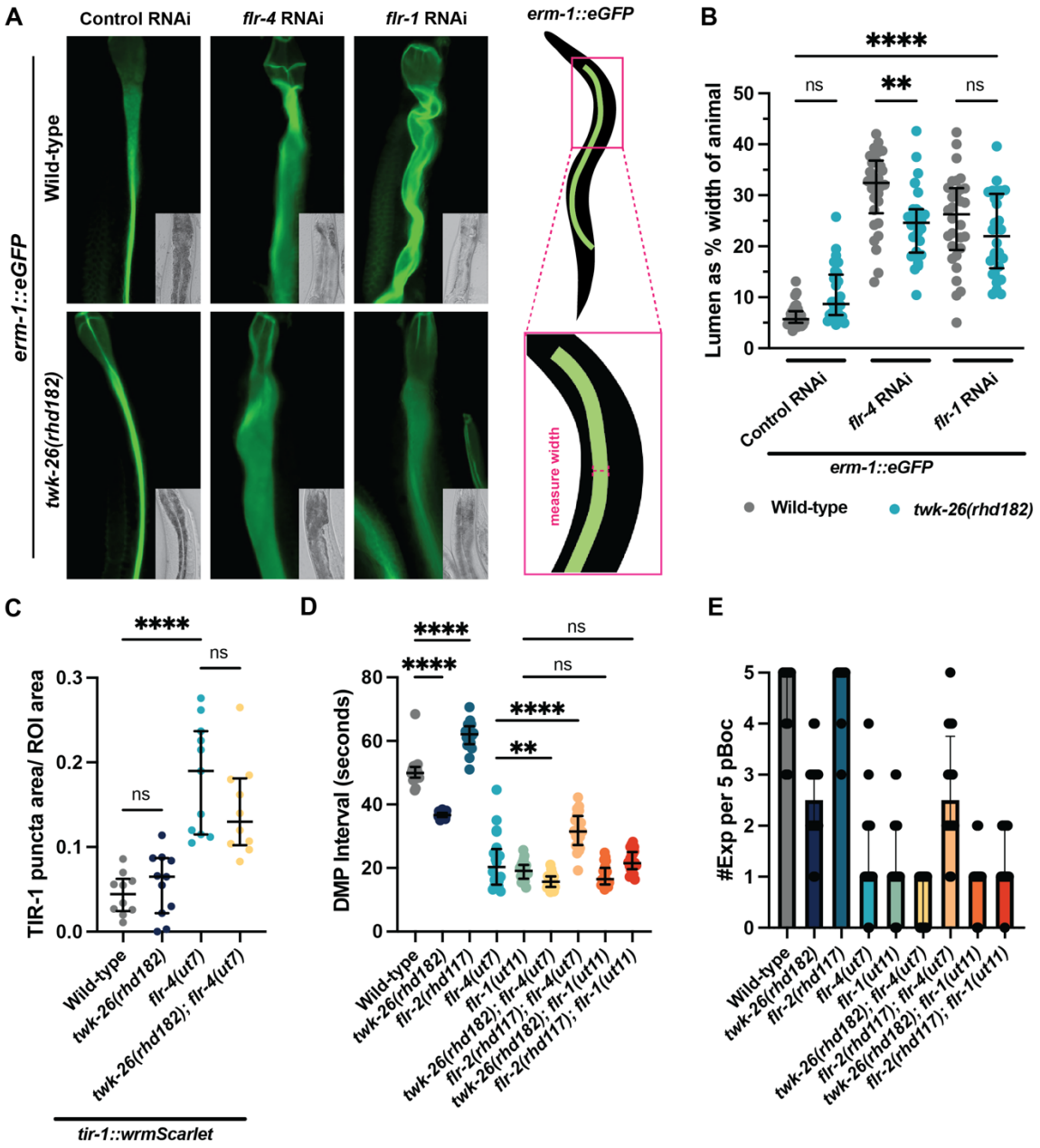

Figure 5. The *twk-26* gain-of-function mutation fails to suppress the intestinal morphology and defecation defects of the *flr-4* and *flr-1* mutants.

(A) Representative fluorescence images and inset DIC images of ERM-1::GFP or ERM-1::GFP*; twk-26(rhd182)* day 1 adult animals subjected to control, *flr-4*, or *flr-1* RNAi. The ERM-1::GFP protein marks the intestinal lumen. (B) Quantification of lumen width as a percentage of body width at the measurement site (median and interquartile range; ns, not significant, **, P=0.0039, ****, P<0.0001, one-way ANOVA). (C) Quantification of TIR-1::wrmScarlet puncta size in the posterior intestine of the indicated strains as day 1 adults. Data are presented as median and interquartile range (ns, not significant, ****, P<0.0001, one-way ANOVA). (D) Measurements of the average time interval between posterior body wall contractions (pBoc) (5 pBoc events recorded per animal). Each data point represents the average DMP interval of an individual animal (median and interquartile range; ns, not significant, **, P=0.0014, ****, P<0.0001, one-way ANOVA). (E) The number of pBoc events that were accompanied by intestinal expulsion (Exp) across 5 observed pBoc intervals. Data are displayed as the median (the bar height) with interquartile range (error bars). (D, E) 10 animals were scored for two independent experiments for a total of 20 animals per strain (strains contain *rhdSi42*).